ISSN: 2997-6170

Research Article

Space Science Journal

Mesoscale and Large-Eddy Simulation of the Boundary-Layer Process of Cumulus Development over Naqu, Tibetan Plateau Part B: The Low-level Baroclinic Vortex and its Contribution to Cumulus Clouds Formation

B. Kpaikpai[1, 3, 4], J. Sun[1]*, J. Zhu[2,3], M. Banna[5], E. Panassa[4] and D. Kakpa[6]

[1]*Key Laboratory of Cloud-Precipitation Physics and Severe Storms (LACS), Institute of Atmospheric Physics (IAP), Chinese Academy of Sciences (CAS), Beijing, China.*

[2]*Key Laboratory of Geophysical Fluid Dynamics, IAP, CAS, China.*

[3]*University of Chinese Academy of Sciences (UCAS), 100864, Beijing, China.*

[4]*Laboratory of Ocean and Atmosphere Interaction, Department of Physics, Faculty of Science and Technology, University of Kara, Kara–Togo*

[5]*Laboratory of Physics, Energy, Thermal and Mass Transfers, Department of Physics, University of Lome, Lome – Togo.*

[6]*Benin's National Meteorological Agency, the Ministry of Living Environment and Transportation Responsible for Sustainable Development. Cotonou Benin.*

***Corresponding Author**

Jiming Sun, Key Laboratory of Cloud-Precipitation Physics and Severe Storms(LACS), Institute of Atmospheric Physics (IAP), Chinese Academy of Sciences (CAS), Beijing, China.

Submitted: 2024, Jul 02 **Accepted:** 2024, Jul 26 **Published:** 2024, Jul 31

Citation: Kpaikpai, B., Sun, J., Zhu, J., Banna, M., Panassa, E., et al. (2024). Mesoscale and Large-Eddy Simulation of the Boundary-Layer Process of Cumulus Development over Naqu, Tibetan Plateau Part B: The Low-level Baroclinic Vortex and its Contribution to Cumulus Clouds Formation. *Space Sci J, 1*(2), 01-15.

Abstract

The Tibetan Plateau's vortices and internal forcing elements interact to form cumulus clouds in the Naqu area. The study has examined the physical mechanism of the interaction between the low-level baroclinic vortex that forms within the large-scale convergence zone (33°–36°N and 84°–94°E) and the deep cumulus cloud during the Day 3 of the model experiment. The purpose was to advance our understanding of the ABL process of cumulus development over Naqu. Analysis for the study was done using the simulation results from Part A's Scenarios B and C. The findings imply that deep cumulus cloud formation required the development of a low-level baroclinic vortex within large-scale convergence zones. Additionally, the positioning of the Subtropical Jet at 36°N and the presence of the South Asian High impacted both the vortex and the resulting cumulus cloud types. In addition, a microphysical analysis indicates that the cloud, ice, snow, and graupel formations in Scenario B imply the production of cold rain through a mixed-phase process. In contrast, the presence of cloudy liquid water in Scenario C supports the dominance of warm rain in the process. Our study highlights the significance of mixed-phase processes as the primary source of uncertainty in the WRF-LES model and recommends further investigation into the planetary boundary-layer scheme utilized in both mesoscale simulation and LES. To improve the dependability of our findings, we advise Scenario B to impact scientific research outcomes by utilizing the most recent planetary boundary-layer schemes and raising both horizontal and vertical grid spacing.

Key Points

- A low-level baroclinic vortex, southerly winds, Subtropical Jet, and South Asian High interact to influence cumulus development over Naqu.
- The Low-level wind advection and large-scale forcing have an important impact on cloud dynamic properties over Naqu.
- WRF-LES provided accurate estimates of cumulus development, highlighting the need for improved dynamic-microphysics interaction over Naqu.

1. Introduction

The atmospheric boundary layer (ABL) over the Tibetan Plateau (TP) is uniquely characteristic due to its location on the highest orography in the world [1,2]. It has the potential to either suppress or enhance heavy rainfall and severe thunderstorms, among other weather phenomena. The TP region is a very complex terrain where the ABL exerts a profound thermal and dynamic influence on the local and even global atmosphere [2–6]. The Naqu area of the TP is notably an interplay of physical mechanisms influencing the ABL process and challenging the prediction of the deep cumulus development. The well-known phenomena of the ABL process on the Naqu area are the mechanism associated with the TP's vortices [7–10]. The TP vortices develop as a result of thermal forcing [1,7,9,11,12]. The low-level baroclinic vortex in TP, often called the heavy precipitation vortex, is believed to play a significant role in the East Asian water cycle [7–9]. Although TP vortices have been observed and analyzed extensively, numerical prediction work on them has not received much attention. The exponential growth of numerical prediction models in weather forecasting and scientific research emphasizes the importance of reexamining the mechanisms of the low-level baroclinic vortex in the mesoscale model. In addition, Li et al. [13] and Ding et al. [14] revealed that warm and wet events have notably increased over the TP. The latter authors emphasized that the temperature in summer has been increased at a rate of 0.026 ° C per year in the previous four decades, particularly in eastern TP. Consequently, TP experienced a decrease in snow cover, loss of ice mass, increased river runoff, and altered hydrological processes [15–18]. Deep cumulus clouds are critical to the water cycle. Temperature and moisture are two examples of environmental factors that influence them. This highlights the need for additional research into the deep cumulus process. This research aims to advance our understanding of the ABL process of cumulus development over the Naqu area in TP.

According to Chen et al. [19], the sensible heat flux (HFX) has a significant impact on cumulus cloud formation over the TP. Flohn [20] previously noted that in summer, the TP highlands function as a heat engine, creating a significant convective chimney in the southeast, where giant cumulonimbus cells continuously transport heat into the high troposphere. Four decade later Wu et al. [11] emphasized that sensible heating on the sloping side surfaces of the plateau, called the sensible-heat pump, is a driving source of the southern meridian circulation. The latter study pointed out that the warm air particles that rise in the summer above the TP pull air from below and air from around the lower troposphere, which converge towards the TP area and rise on heated sloping surfaces. The latter study named this process as conditional instability of the second kind (CISK) and confirmed one decade later by Zhao et al. [21]. CISK is a process by which low-level convergence in the wind field produces convection and cumulus clouds, thereby releasing latent heat [22–28]. The changes noted in surface temperature would indicate a modification in the formation of the local cumulus clouds, underscoring the substantial link between the warming of the Earth's surface and the development of cumulus clouds [29–31].

For instance, Tingyang and Reiter [32] found that in the TP area, cloud condensation rates, liquid water content, and precipitation efficiency are lower than in adjacent areas. Twenty years later, Sato et al. [33] found that convective clouds over TP during the day tend to have a smaller horizontal scale than a resolvable mesoscale resolution and suggested further study with a finer grid resolution of less than 7 km. Based on satellite observations, Luo et al. [34] showed that cumulus convection is shallow over TP. Despite challenges in understanding ABL processes in the Naqu area, the TP atmospheric science experiment (TIPEX-III) campaign employed integrated remote sensing tools such as lidar ceilometer, and Fengyun satellite images, whose data were used to ensure the model's ability. They emphasized two predominant cloud bases at average elevations of 2 km and 6 km above ground level (AGL). They have further detected a deep cloud reaching up to 16.5 km in depth. They recommended further modeling research into TP cloud physics to enhance our comprehension of these phenomena.

Apart from these changes, some controversies would have left doubts about what was already acquired when referring to cumulus development. For instance, Dong et al. [36] suggested that during the Summer Asian Monsoon, a large-scale ascent over the Indian subcontinent moves moisture and hydrometeors southwest of Naqu. By contrast, Zhao et al. [21] highlighted that cumulus clouds form around the TP, regardless of intrusive effects. The latter authors have, however, identified TP's vortices as the primary mechanisms regulating deep cumulus cloud formation in preflood season in southwestern TP. Our study is dedicated solely to the cumulus phenomena resulting from the formation of low-level baroclinic vortices.

The TP's vortex is a low-pressure system that develops over the plateau in July and August, most notably observed at the 500 hPa level. According to Feng et al. [7], the genesis area of the low-level baroclinic vortex is collocated with the large-scale convergence zone, bounded by 33–36°N, 84–94°E, northwest of the Naqu site. The latter vortex has an average lifespan of 15 hours and a mean horizontal dimension of 280 km with a transition speed of 10 ms^{-1}. The Low-level Jet (LLJ) and weak mid-level trough over the large-scale convergence zone at the presence of the South Asian High (SAH) aloft are the precursors to the low-level baroclinic vortex. The low-level baroclinic vortex influences the cumulus clouds by moving towards eastern China, where it causes extreme rainfall and flooding [7,9,10]. The subtropical jet (STJ), typically flowing near 40°N in summer, often shifts convective storms toward the downstream area [33,35,37]. Obviously, the STJ, is the cause of the eastward moving of the low-level baroclinic vortex [38,39].

The SAH, is a planetary circulation of the anticyclonic wind in the upper troposphere [40–42]. It stretches in summer alongside the Iranian plateau (IP) to TP, including surrounding areas, and has a quasi-biweekly variability. Due to the adiabatic compression, the SAH forces the westerly flow blowing north of it to deflect downstream [38]. The northeasterly wind at upper levels south of the SAH promotes subsidence in that area. Sato [43] and Chen et al. [44], investigated the sub-seasonal intensity variation of

the SAH in relationship to diabatic heating using observation and coupled model intercomparison project (CMIP5). The latter authors found that SAH generates the positive and negative vortex anomalies in the lower and upper troposphere accompanied by an upward motion anomaly. They have further shown that more substantial warming of the TP leads to the strengthening and eastward extension of the SAH, which causes an increase in southwest moisture transport and convergence downstream side. Tingyang & Reiter [32] suggested that the stability of SAH in summer would be associated with the heating of the large-scale environment above the TP region. The SAH and STJ affect the development and maintenance of deep cumulus clouds, with a low-level baroclinic vortex further influencing this process [37,38,38,41,43,45–48].

From the 1970s to 2014, three scientific experiments, including TIPEX-III, advanced our understanding of clouds physics and mesoscale circulation on the TP region [35,39,49,50]. The stated drawback of predicting deep cumulus clouds underscores the limitations of our current understanding. At the same time, the accuracy of forecasting models in representing weather in TP is of significant concern. Wang et al. [51] highlighted that TP and Asian land warming, large-scale forcing, global warming, aerosols, and land surface conditions all exert large and complicated effects on precipitation changes on TP. Fu et al. [49] emphasized that our understanding of the mesoscale system on TP and its interpretation on a physical basis is limited because of insufficient observation data. Feng et al. [10], Ma et al. [52] , and Son et al. [53] have proposed a carefully planned observation program to supplement new findings on the characteristics of convective processes on TP.

Despite challenges in understanding ABL processes in the Naqu area, the TIPEX-III campaign employed integrated remote sensing tools such as lidar ceilometer, and Fengyun satellite images, whose data were used to ensure the model's ability. Kpaikpai et al. [54] showed that observation nudging approach can efficiently capture cumulus cloud patterns. The WRF-LES, which has turbulence-resolving capabilities within the WRF framework, was useful in this study. Kpaikpai et al. [54] focused on comparing observation data to simulation results.

The study's objective is to assess the interaction between the low-level baroclinic vortex that forms in the large-scale convergence zone (33–36°N, 84–94°E) and cumulus clouds on the Day 3 of the model experiment using the Scenarios B and C from Kpaikpai et al. [54]. The research further illuminated the WRF-LES model's reactions to certain microphysical characteristics. Substantial boundary-layer turbulence and cumulus clouds were observed across Southeast Asia during the model experiment. The supplementary file has a video of Fengyun's two-dimensional satellite image attached. The next sections are organized as follows: Section 2 covers investigation metrics; Section 3 explains the physical mechanism underlaying the cumulus development; Section 4 analyzes WRF-LES model responses to microphysical traits; and Section 5 presents conclusions.

2. Metrics For Investigation

2.1 Helmholtz Decomposition of the Horizontal Total Wind Vector

We investigated the low-level baroclinic vortex using a two-dimensional Helmholtz decomposition of the horizontal total wind vector into divergent and rotational modes. Equation (1) provides a theoretical consideration of this decomposition, which is well documented in the literature [58-61].

$$\boldsymbol{V} = \boldsymbol{K} \cdot \boldsymbol{\nabla\psi} + \boldsymbol{\nabla\chi} \tag{1}$$

where ψ is the stream function obtained for irrotational flow, χ the velocity potential, K is the local unit normal vector, and ∇ (Nabla) the horizontal gradient operator. The stream function represents the solenoidal component of the two-dimensional Helmholtz's decomposition of the horizontal total wind vector, while the velocity potential represents the irrotational part [62]. The stream function and velocity potential are determined as the solution of Laplace's equations satisfying Equations (2) and (3), respectively [63-66].

$$\boldsymbol{\zeta} = \boldsymbol{\nabla^2\psi} = \boldsymbol{K} \cdot \boldsymbol{\nabla} \wedge \mathbf{V} = \mathbf{0} \tag{2}$$

$$\boldsymbol{\delta} = \boldsymbol{\nabla^2\chi} = \boldsymbol{\nabla} \cdot \boldsymbol{V} = \mathbf{0} \tag{3}$$

where, ζ is the vorticity and δ the divergence. In current decomposition, the divergence and vorticity are first estimated using spherical harmonics [63,65,66], thereafter the divergence and vorticity are set to zero, respectively to obtain the vorticity potential and the stream function. Latter is used to derive the divergent and rotational wind components [67]. The relevance of rotational and divergent modes of motion and their interplay in this study is that this approach contributes to an improved understanding of the dominant interaction mechanism that governs the ABL processes of the cumulus cloud development. Bierdel [67] has shown that divergent and rotational components of the horizontal total wind vector, and their interaction, are crucial to understanding the characteristics of real mesoscale atmospheric flow field. The latter wind components are used to explain how solar radiation processes affected the thermal state of the mesoscale circulation over Naqu on day three of the model experiment.

2.2. Estimation of the Surface-Atmosphere Interaction on Day 3

To understand the wet process of the ABL driving cumulus clouds during the lifting and condensation and fusion processes, thermodynamics properties affecting cumulus cloud development are calculated at a given temperature (T), pressure (P) and velocity components using: the mean pressure fluctuation ($\overline{P'}$); mean pressure vertical velocity ($\overline{\omega}$); the mean buoyancy; turbulence kinetic energy (TKE), which is the contribution of the velocity variances in the zonal ($\overline{u}^2$), meridional ($\overline{v}^2$), and vertical ($\overline{w}^2$) directions, respectively; wind shear (WDS); ABL kinetic flux of heat $(\overline{w'\theta'_{lv}})$, and ABL kinetic flux of moisture $(\overline{w'q'})$; the variance of latent heat of vaporization ($\overline{L'}$). Given the ABL variables X and Y, the covariance is given as in Equation (4) [68–71]. The latter is used to compute the kinetic fluxes and the variances."

$$\overline{X'Y'} = \frac{\sum_j^N (X_j - \bar{X})(Y_j - \bar{Y})}{N-1}, \quad (4)$$

where, $X_j = \bar{X} + X_j'$ and $Y_j = \bar{Y} + Y_j'$, the overbar represents the mean values, calculated over 1 hour and 48 minutes from 15:00 to 16:48 BT, the prim (‘) denotes perturbation value, which is simply the difference between the variable and the mean value; N is the number of samples. The thermodynamic quantities u,v,w and θ_{lv} are given as in Equations (5-8) and detailed in [68-74].

$$\boldsymbol{\theta_{lv} = (1 - 0.608 r_v) T \left(1 - \frac{L_v r_l}{C_{pd} + r_t C_{pv}} \frac{1}{T}\right) \left(\frac{P_0}{P}\right)^{\mathcal{K}}}, \quad (5)$$

$$\boldsymbol{L = \left(m_d C_{pd} + m_t C_l\right) T + m_v L_v}, \quad (6)$$

$$TKE = \frac{1}{2}\left(\overline{u'}^2 + \overline{v'}^2 + \overline{w'}^2\right), \quad (7)$$

$$\boldsymbol{B = g \frac{T_{vc} - T_{ve}}{T_{ve}} \approx g \left(\frac{T'}{T} - \frac{P'}{P} + 0.608 r_v' - r_t\right)}, \quad (8)$$

where, the subscripts c and e denote cloud and the environment, respectively; g is the gravitational acceleration; L_v represent the specific latent heat of vaporization; C_{pd}, C_{pv} and C_l are, respectively the isobaric specific heat capacity of dry air, water vapor, and liquid water; K=0.2854(1-0.24r_v) represents the Poisson constant for moist air ; r_v and r_l stand for the water vapor mixing ratio and liquid water mixing ratio, respectively; $m_t = m_d r_t = m_d(r_v + r_l)$ represents the net mass of the water subsidence; z is the altitude. Note that θ_{lv} is used in this study in its simplified form, assuming that r_l tends to zero. This is because in the heterogeneous system, $\mathbf{r_l}$ and ice mixing ratio ($\mathbf{r_i}$) are negligible, while the isobaric change in enthalpy is calculated as latent heat. Emanuel [68] assessed that the moist enthalpy consists of the specific enthalpies of dry air, water vapor, and liquid water. A similar approach has been used by Zhou et al. [75] to simulate the microphysics and their influencing factors in a shallow cumulus.

2.3. Calculation of Liquid Water Path

Calculation of the hydrometeor liquid water path (LWP) was performed in this study. LWP mentioned here represents the integral of the liquid water content (LWC) of hydrometeors over the entire depth of an atmospheric column, as given in Equation (9); the theoretical basis of LWP is given in [76-78].

$$\boldsymbol{LWP = \int_0^z \rho_i \cdot \mathbf{Q} \cdot dz}, \quad (9)$$

where, q represents the hydrometeor type (cloud, ice, rain, snow, or graupel), ρ_i is the density of the moist air, and z = 12 km AGL is the model level of integration [79,80]. LWP is expressed here in g/m^2. The treatments of the LWC can be found in Pruppacher and Klett [81].

3. Physical Mechanism of Cumulus Development

3.1 Wind Characteristics and the Low-pressureTroughs

The horizontal characteristics of the wind and the geopotential height are the precursors of the forthcoming weather. Note that the environmental factor that has more influence on ABL processes is the wind speed. We examined the air temperature, wind flow field and the geopotential height from Scenario B at four critical horizontal levels that affected ABL processes, possibly by mesoscale and large-scale forcing on the Day 3 day of the model experiment. These levels include 800 m (~460 hPa), 1.5 km (~450 hPa), 4 km (~300 hPa), and 8 km height AGL (~200 hPa).

The geopotential height can be used to analyze the large-scale influence on the ABL processes of cumulus cloud development by examining the position of troughs and ridges. High geopotential height indicates a ridge and quiescent weather. In contrast, a low geopotential height suggests a storm or trough in the mid-troposphere levels. In meteorology, a trough is referred to as an elongated region of relatively low atmospheric pressure. Since low pressure implies a low height over a pressure surface, troughs and ridges refer to features in the same sense as on a topographic map. A trough is the result of the movement of the air in the atmosphere. In the current case simulation, the initialized ABL wind and low geopotential high characteristics 6 hours before the cumulus cloud development are depicted in Figure 1.

At 460 hPa, Figure 1a shows the low air temperature (shaded) over the plateau with snow in some zones where the wind converges. The wind blows from the high-pressure zones to the low-pressure ones. We can see an active LLJ between 88° and 90°E, blowing from the south to the large-scale convergence zone. The LLJ is known to carry warm and humid air across Naqu. The large-scale convergence zone likely has a freezing temperature that facilitates heat transport to those areas.

At 450hPa level, Figure 1b also shows an active LLJ between the 88° and 90°E, blowing meridionaly as in Figure 1a. Moreover, a low geopotential height (black lines) can be seen at the outskirts south, east, and north of the Naqu area, indicating the low-pressure trough within the zone limited by the low geopotential height lines. Specifically, the low geopotential height lines are much closer to each other at the upper reach of the southern plateau slope. Lows near the surface are elongated areas of low pressure and represent surface convergence and rising air, often leading to clouds and precipitation. The low-pressure trough in the southeast zone of Naqu site (Figure 1b) also indicates another source of meridional circulation. There is a low-level southeast wind blowing towards the large-scale convergence zone. We can also see an anticyclonic rotation of the horizontal wind vector initializing northwest of the LLJ. At the southeast of LLJ there is a ridge, indicating quiescent weather.

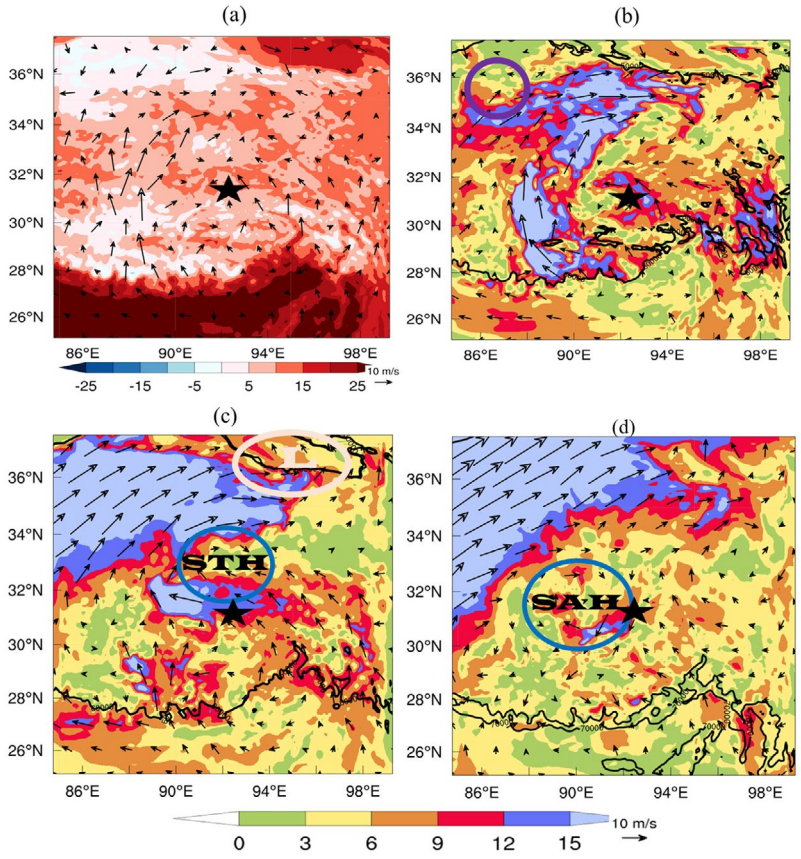

Figure 1. Tracer initialized 6 hours earlier on July 19, 2014, at 10:45 Beijing Time (BT) depicted over $\mathbf{D0}_{i=1}$: (a) Air temperature (°C) and wind speed (ms^{-1}) at the first model level (shaded), approximately 17 m above ground level (AGL) or 460 hPa level from Naqu observatory; (b), (c) and (d) are wind speed (shaded) and wind vector at 450 hPa, 300 hPa and 200 hPa, respectively, The zone of temperature <5°C in (a) represent the low pressure zone; STH, subtropical high; SAH, south Asian high; The black stars indicate the location of the Naqu (31.483°*N*,92.067°*E*) site.

At 300hPa level, Figure 1c shows nothrwesterly wind with relatevily high speed as compared to other areas and blowing north of Naqu site. This possibily refers to the STJ. As mentioned earlier in this study, the fast-moving air currents in STJ transport weather systems across the TP toward the downstream area, affecting temperature and precipitation. The STJ intensifies the ridge to the south and the low to the north of this zone as it passes across the large-scale convergence zone. As shown in Figures 2a and 2b, the ridge on the right side of the LLJ is the subtropical height (STH). The STH causes the LLJ to deflect right and sink within the large-scale convergence zone.

At 200 hPa, Figure 1d shows northwesterly STJ deflected north at the upstream and southward downstream due to the existence of the SAH around the Naqu observatory. We mentioned earlier that the SAH is a planetary circulation of the anticyclonic wind in the upper troposphere over TP. The SAH acts as a barrier to vertical convection. We can see that the air is relatively calm from the Indian subcontinent to the south of the STJ lower boundary.

In summary, the circulation pattern discussed above is consistent with the regional climatology that Feng et al. [7] described. The LLJ, the low-pressure trough, and the SAH are all part of the heavy precipitation vortex formation mechanism discussed earlier in this study. Also, note that low and high are consequences of low-level baroclinic instability. To further our understanding of the circulation pattern that led to the deep cumulus, we decompose the total wind vector into rotational and divergent components, which we have presented in the next section.

3.2. Vortex Development and Interaction with the Meridional Circulation

This section uses the divergent and rotational modes of the horizontal total wind vector to examine the mesoscale circulation that characterized the weather on July 19, 2014. Analysis revealed a low-level baroclinic vortex affecting cumulus cloud development over Naqu. Figure 2 depicts the divergent and rotational components of the total wind vector, along with their respective velocity potential and stream function. The rotational wind component rotates clockwise around positive stream values, indicating subsidence, and counterclockwise around negative values, signaling upward motion.

Figure 2a depicts a convergence zone spanning 33°–36°N and 84°–94°E, which is the large-scale convergence zone. As shown in Figures 2b, 2c, and 3d, subsidence dominated the stream at the southwest and southeast, respectively. Two centers of the STH

can be seen in these figures. A negative stream exists between the two STHs (Figures 2b and 2c), which is conducive to the convection of cumulus clouds. There is also a low-pressure trough in the convergence zone, which we named earlier in this study the low-level baroclinic vortex (Figures 2b and 2c). The STH center in the southeast drives the northward advection of the meridional circulation, allowing southeast upslope winds to converge towards the Naqu area. The southwest-based STH advected the low-level baroclinic vortex southeastward. Figure 2e shows the SAH within the positive stream function at 200 hPa. A baroclinic vortex and meridional circulation can enhance deep convection due to strong wind shear in their interaction. The animation of the Fengyun 2D satellite images indicates a big anticyclonic rotation at the top of the cloud. The SAH is elongated zonally and aligned vertically with the vortex. In the current case simulation, all the conditions described by Feng et al. [7] for the low-level baroclinic heavy rain vortex were satisfied.

The analysis shows that the convergence in this simulation is due to the low-level baroclinic heavy rain vortex and meridional circulations. The particularity of this type of vortex is its low-level baroclinicity in interaction with the SAH. In the current case study, this vortex moves eastward under the effect of the STJ and then deflects southward under the influence of the clockwise rotation of the west STH of the two SAH activities. Note that the meridional circulation wind concerns the LLJ west of the Himalayan sector and that of the east sector. The LLJ west of the Himalayas provides the humid air that creates the low-level baroclinic vortex. The eastern one goes ahead with the north wind, blowing from the deflection of the low-level baroclinic vortex. This last front led to deep cumulus clouds in that zone. However, the adiabatic compression of the SAH limited the cumulus cloud depth to some vertical extents. The Naqu site experienced subsidence from the STH, located to the west.

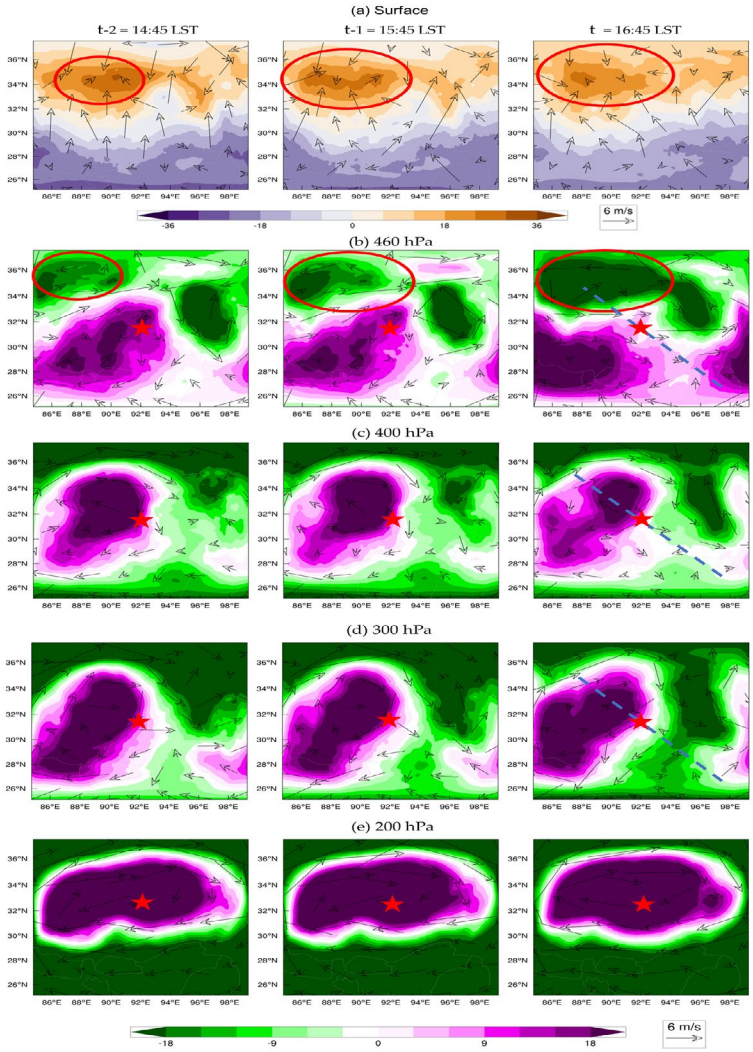

Figure 2. (a) The divergence wind component of the total wind vector overlays the shaded velocity potential; the negative values denote divergence, whereas the positive values represent convergence. (b)–(e) represent the rotational wind component of the total wind vector and the shaded stream function; the negative stream values correspond to low-pressure troughs, whereas positive values represent high-pressure ridges. LST refers to local standard time (Beijing Time). The horizontal maps are from $D0_{i=1}$, and Figure 3's vertical cross sections align with the antidiagonal dashed lines. A video showcasing Fengyun's 2D satellite images of a large anticyclone over the Tibet Plateau has been attached.

3.3. Cumulus Development on Day 3 of the Model Experiment

Vertical cross-sections of humidity, temperature, wind flow, shortwave and longwave heating rates, and liquid water content help describe the initiation and growth of cumulus clouds. We analyzed vertical cross-sections from Scenario B, which showed the best mesoscale simulation per Kpaikpai et al. [54]. We can see in Figures 4b and 4c that deep cumulus convection developed southeast of the region over the hills, where the LLJ and easterly wind played, respectively, a role in entrainment and detrainment. We found the LLJ above the freezing level at around 1.5 km AGL. The LLJ transported moist air northeast, facilitating the formation of cumulonimbus clouds.

Figure 3a shows the high relative humidity, near 100%, connected to the LLJ, while Figure 3b illustrates the longwave radiation absorption zone. Figure 3b shows a high absorption rate of longwave radiation in optically thick clouds at vertical depths greater than 9 km AGL. At the top of the convective core, especially at 3 and 9 km AGL, cloud droplets scatter incident shortwave radiation, causing a high heating rate (Figure 3c). As illustrated in Figure 3e, the deep cumulus cloud grew locally in the area with high elevations.

During the daytime peak, moist air from the LLJ reached saturation at 6 km AGL, resulting in cumulus cloud formation due to condensation. Figure 3 shows that easterly winds significantly detrained clouds at the upper level. Cloud mass from detrainment formed the upper cloud layer above 6 km AGL. We found that the convective core lasted for more than 4 hours from the diurnal peak to the late evening, allowing the anvil clouds to detrain from the convective core until the convective core died down. The cloud mass concentration (Qc) was estimated to be high in boundary layer clouds, particularly in the entrainment region, and this has led to increased precipitation from the ABL could during the model experiment. Thus, the inflow cumulus cloud could not grow vertically due to the influence of the easterly wind (Figure 3e). The results are consistent with the theory of Tingyang and Reiter [32] that the residual mass flux in an active cumulus cloud is generally directed downward. The result is also consistent with the finding by Yan et al. [82] that a strong layer of net radiative cooling of clouds at 8 km hinders cumulus clouds from growing vertically. Provided that the outcomes of our analysis remain within the confines of low-level baroclinic vortex dynamics, we can assert that our research aligns with Zhao et al. [39] findings that cumulus develops locally on TP and does not originate from elsewhere.

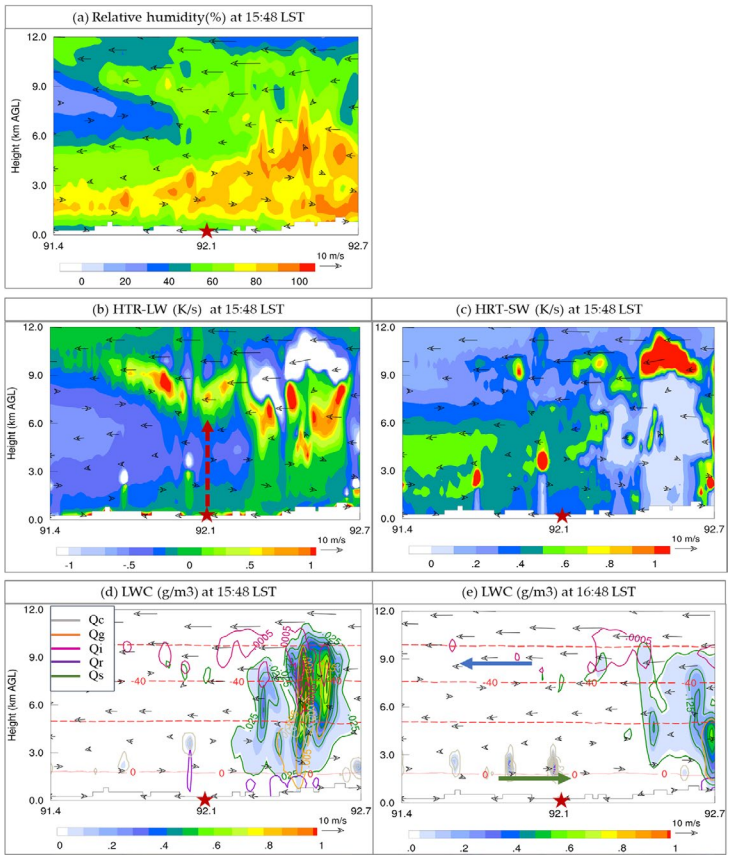

Figure 3. Vertical cross-sections from Scenario B along the antidiagonal (refer to Figure 2b): (a) relative humidity (RH); (b) and (c) heating rates from shortwave radiation (HTR-SW) and longwave radiation (HTR-LW), respectively; (d) and (e) Hydrometeor water content (LWC) ($g \cdot m^{-3}$), with shading indicating total LWC from $D0_{i=1}$ and $D0_{i=2}$, respectively. The hydrometeor types include cloud (Q_c), graupel (Q_g), ice (Q_i), rain (Q_r), and snow (Q_s). Solid red lines indicate positive temperature (°C), while dashed lines indicate negative temperatures. Vectors illustrate wind fields based on zonal and vertical velocities. The blue arrow indicates upper-level cumulus cloud detrainment, the green arrow represents low-level cumulus cloud entrainment, and the red arrow shows a radar observation schematic at Naqu (marked by the red star).

3.4. Surface-Atmosphere Interaction on Day Three

This section demonstrates how the STJ, SAH, land-surface temperature, and upslope wind convergence alter local conditions to promote cumulus convection. The discussion focused on 4 meteorological stations, objectively chosen. These stations are as follows: Yituohe (34.21°N, 92.43°E), located north of STH within the low-level baroclinic vortex; Naqu (31.483°N, 92.01°E), located at the eastern outskirts of STH; Lhasa (29.667°N, 91.133°E), located south of the Naqu site, within the low-pressure trough, outside the STH; and Rikaze (28.663°N, 87.08°E), located southwest of SAH. The analyses are shown in Figure 4.

The liquid water virtual potential temperature, $\boldsymbol{\theta}_{lv}$ (Figure 4a) is conserved in the reversible moist adiabatic process. It has the advantage of returning to the dry potential temperature in the absence of liquid water. The virtual potential temperature and $\boldsymbol{\theta}_{lv}$ are analogous, while it has been demonstrated that there is no big difference between the two latter quantities (83,84). As shown in Figure 4a, the $\boldsymbol{\theta}_{lv}$ increases monotonically at all meteorological stations, indicating a stably stratified atmosphere. A stably stratified atmosphere generally suppresses vertical motions associated with turbulence.

Profiles of buoyancy, vertical velocity, and latent heat provide insights into the mechanisms sustaining shallow cumulus clouds during the model experiment. The way to assess the atmosphere's stability is to consider the vertical motion of an air parcel from its equilibrium position. The buoyancy is shown in Figure 4b. The buoyancy increases gradually near the surface to about 2 km AGL. Then it decreased gradually between 2 km and 8 km AGL and increased again from 8 km to its highest value at 12 km AGL for each station, indicating that the parcel displacement was stable. While, except for Rikaze station, the buoyancy was negative at all stations below 1.5 km AGL, indicating the unstable displacement of the parcel and where the parcel transited through its neutrally stable condition. Buoyancy within the cloud layer is suppressed. In this simulation, the cloud layer ranges from 2 km to 8 km above ground level.

The vertical velocity (Figure 4c) for all stations can be classified into two groups based on whether the parcel velocity changed from negative to positive below or above the level where the buoyancy force changed from negative to positive. However, this condition meets the case of Altocumulus. According to Lu et al. [85], the mean buoyancy of a single cloud must be greater than 0.005 ms^{-2}. In this analysis, the minimum buoyancy within the cloud layer is 0.023 ms^{-2}, greater than the threshold value. So, instead of referring to the buoyancy force's sign change, we can use the threshold value. In addition, the groups can determine whether the buoyancy force can approximate the vertical velocity trend during the stable displacement of a parcel. The buoyancy forces of the Lhasa and Yituohe stations are found to approximate the trend of their velocities, respectively. At each of the two stations, the height at which the vertical velocity first changes the sign exceeds the height at which the buoyancy force changes the sign. Under these conditions, Newton's laws of motion have been verified. This is because the STH does not influence these stations, while the SAH has a minimal impact on the two stations. Naqu station has a negative vertical velocity above 2 km AGL, whereas Rikaze station has a negative velocity above 1 km AGL, indicating subsidence in their respective areas. The Naqu station, in particular, is located within the SAH-influenced boundary.

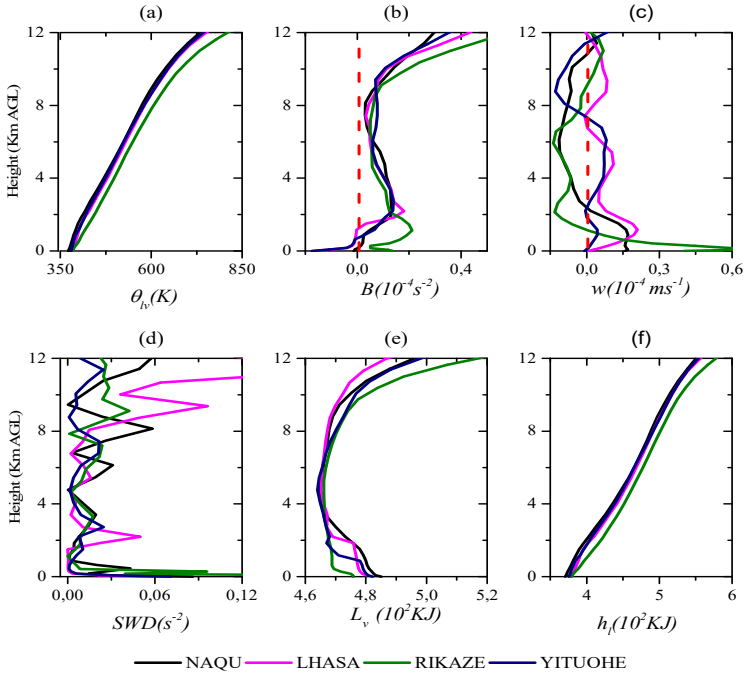

Figure 4. Vertical profiles from the parent domain, depicted over four stations including Naqu1 (31.483°N,92.067°*E*), Lhasa (29.667°*N*,91.133°*E*), Rikaze (28.663°*N*,87.08°*E*) and Yituohe (34.21°*N*,92.43°*E*): (a) Liquid water virtual potential temperature (θ_{lv}); (b) Buoyancy (B); (c) Vertical velocity; (d) wind shear squared (SWD); (e) Latent heat of vaporization (L_v); Liquid water static energy (h_l).

The release of latent heat occurs when water vapor condenses or liquid water freezes. The latent heat is consumed as the ice melts or liquid water evaporates. The latent heat of vaporization is illustrated in Figure 4e. It is found that the latent heat is positive for all stations and decreases gradually from the surface to about 5 km AGL, where it increases again gradually from 5 km to 8 km AGL, where it increases faster. This explains why freezing and condensation dominate within the ABL below 5 km AGL. Evaporative cooling is prominent above 8 km AGL at all stations. It must be noted that condensation occurs faster near the surface for Rikaze and Yituohe. Yituohe is located at the leading edge of the strong southerly upslope wind, whereas Yituohe station is collocated with the surface convergence zone. Surface convergence leads to upward motion. The evaporative cooling is also faster in the latter two stations' profiles beyond 5 km AGL. This is due to the STH and SAH's influence on the Rikaze station from the middle to upper troposphere, whereas the STJ position and, most likely, the SAH influence the Yituohe station.

In the environment of a nonprecipitating cloud, the static energy (Figure 4f) increases monotonically with altitude. This is because the atmosphere is stably stratified concerning unsaturated parcel displacement (Figure 4a). According to Smith, nonprecipitating cumulus clouds are prone to strong downdrafts caused by mixing with the environment. The hypothesis of shallow cumulus convection in the Naqu area is thus justified.

In support to the analysis of the latent heat release, the vertical wind shear is necessary to determine the vertical structure of the mesoscale convective environment. Figure 4d displays the wind shear. Let's recall the paradigm of Chen et al. [19]. that increasing the wind shear within the ABL strengthens the convective process while weakening the convective process at the top of the convective cloud. As shown in Figure 14d, the shear is found to typically reach its local maximums at all selected stations at 2 km height AGL and above 5 km height AGL. The upper maximum represents the detrainment region due to SAH, while the shear maximum at low altitudes suggests the entrainment layer due to LLJ and where the boundary-layer cumulus clouds developed.

From the above analysis, although there was a good condition for deep convection at the Lhasa and Yituohe observatories, the effect of the internally forced mesoscale process dominated the externally forced mesoscale processes on day three of the model experiment, especially at the middle and upper levels. The situation reversed near the surface for the overall stations selected in this section.

3.5. Dynamic-Microphysical Interaction

The cumulus clouds development is related to a vertical flux of hydrometeors in the atmospheric column. Looking at the profiles of hydrometeors throughout all cloud layers provides insight into the interactions between microscale and mesoscale cumulus cloud processes. Furthermore, comprehensive knowledge of the vertical flux of hydrometeors is relevant to understanding the role of dynamic-microphysical interaction and the strengths and weaknesses of the physical parameterization schemes in the WRF model, eventually. In this section, we examined the hydrometeors mass concentration of the cumulus core and their path, and how the model responded to these features. This investigation concerns Scenarios B and C from kpaikpai et al. [54].

3.5.1. Vertical Profiles of the Hydrometeors Mass Concentration

Clouds are made up of condensed water particles known as hydrometeors. These can manifest as minuscule ice crystals (Q_i), snowflakes (Q_s), hailstones (Q_h) / Graupel (Q_g), or liquid droplets like rain (Q_r) or cloud condensation (Q_c). Figure 5 shows the vertical profiles of the area average of the predicted hydrometeor mass concentration at 16:48 Beijing Time (BT) in each Scenario. This is the mature stage of the observed deep cumulus on Day 3 of the model experiment. According to the results, for each Scenario and hydrometeor type, snow, rain, and cloud particles were more populated (Figures 5a, 5b, and 5d). Graupel and ice mass concentrations are negligible compared to the other hydrometeor types. Thus, our discussion will emphasize the three former hydrometeor types.

In summary, Scenario B generated hydrometeor mass concentration profiles with mostly a single peak, whereas Scenario C's profiles (as shown in Figure 5c) displayed either one or two peaks. For instance, Figure 5b illustrates that peak cloud mass concentrations for both Scenarios occur between 2 km and 4 km AGL. Concurrently, Figure 5e indicates the peak ice mass concentration at 10 km AGL in both Scenarios. In contrast, Scenario C presents two distinct peaks for rain mass concentration (Figure 5a) and snow mass concentrations (Figure 5d). The first peak of rain-type hydrometeors is observed at approximately 1.5 km AGL, with a subsequent peak at 4 km AGL. Similarly, the initial peak for snow-type hydrometeors is near 4 km AGL, with a subsequent one around 9 km AGL in Scenario C. It was also observed that the graupel mass concentration data is absent from the results of Scenario C.

The maximum snow-mass concentration below 4 km AGL in Scenario B, which appears to have two local maximums, originates from the ABL clouds during the entrainment process. The other one from the uppermost layers originates from the detrainment process. By contrast, two local maximums in the profiles of, respectively, rain and snow hydrometeors types in Scenario C indicate that Scenario C exhibits two cloud layers, one within the ABL and the other beyond 6 km AGL with the same origin as in Scenario B. The latter is true because we calculated the area average of the hydrometeor's mass concentrations over domain 5, representing only the area around the Naqu site. This aligns with the outcomes of Scenario B, particularly as illustrated in Figure 3e earlier. This study highlighted earlier that the deep cumulus clouds developed locally in the Naqu area, a little far from the Naqu station. The two cloud layers observed over the Naqu area result from the entrainment and detrainment processes of deep cumulus clouds forming locally to the east of the Naqu observatory. Our explanation may be valid for the two cloud-based that Liu et al. [35] found in their climatological analysis

of clouds and precipitation over Naqu. We should note that low-level cumulus clouds were more populated on July 19, 2019, over the Naqu site in Scenario C. By contrast, Scenario B presented a relatively single layer of deep cumulus reaching 12 km AGL. Indeed, if the process were homogeneous, the results would be independent of the simulation scale. As a result, these findings are likely to point to a limitation in Scenario C, which prevents the complete discovery of the interaction mechanism due to its small simulation domain. A broad field, may miss out on specific details because it focuses on the most important phenomena. Naqu's micro-scale climatology may indicate the presence of two layers of clouds, whereas mesoscale climatology indicates strong convection southwest of Naqu without considering the consequences for the Naqu site. Thus, both scales are necessary for a substantial conclusion.

More cloudy liquid water in Scenario C reveals that warm rain dominates the process. In cloud physics, the warm rain formation process generates precipitation in clouds with sufficient liquid water, updraft, and lifetime to support collision-coalescence growth into drizzle or raindrop sizes. This rain process occurs in shallow cumulus convection, with depths of approximately 2 km. Figure 3e, shown previously in this study, indicates this rain-type process. Meanwhile, cloud, ice, snow, and hail/graupel formations in mesoscale simulation (Scenario B) point to a mixed-phase process that could produce cold rain. It should be noted that the ice crystal process requires a cloud top to cool sufficiently from a high altitude to form the primary ice. Ice crystals are formed through heterogeneous ice nucleation, and their growth produces snow, which can rain and form glaciers. Again, the ice precipitation may melt and form cold rain.

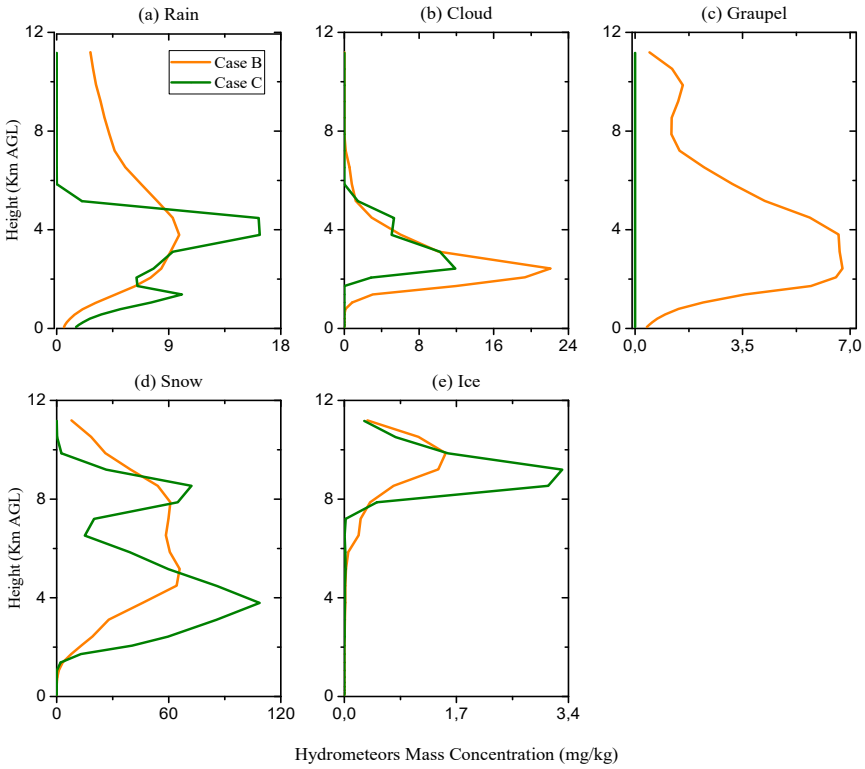

Figure 5. Area average of hydrometeor mass mixing ratio (g/kg) at 16:48 Beijing Time. Case B depicted from $D0_{i=3}$ and case C from $D0_{i=5}$ represent Scenarios in Table 4 of Kpaikpai et al. [54].

3.5.2. Cumulus Hydrometeor's Water Path

The liquid water path (LWP) is one of the most critical variables for modeling the atmosphere. It is essential for understanding radiative transfer. We have computed the liquid water path (LWP), encompassing both liquid and condensed hydrometeor water paths, to bolster the analysis of liquid water content (LWC) and hydrometeor mass concentration. We considered the time frame from 16:00 to 20:00 BT. The calculation results are displayed in Figure 6.

Figures 6a, 6b, and 6d show that the paths of rain, snow, and cloud water were critical in shaping the cumulus cloud over Naqu during the model experiment. The peak hydrometeor water paths appeared six hours earlier in Scenario B than in Scenario C. This makes sense, as the cloud over Naqu resulted from the detrainment from the mature cumulus convective core located southeast of Naqu. The Cloud Water Path indicates a significant flow in the early morning and late evening for Scenario B (Figure 6b), which will require verification in our ongoing studies.

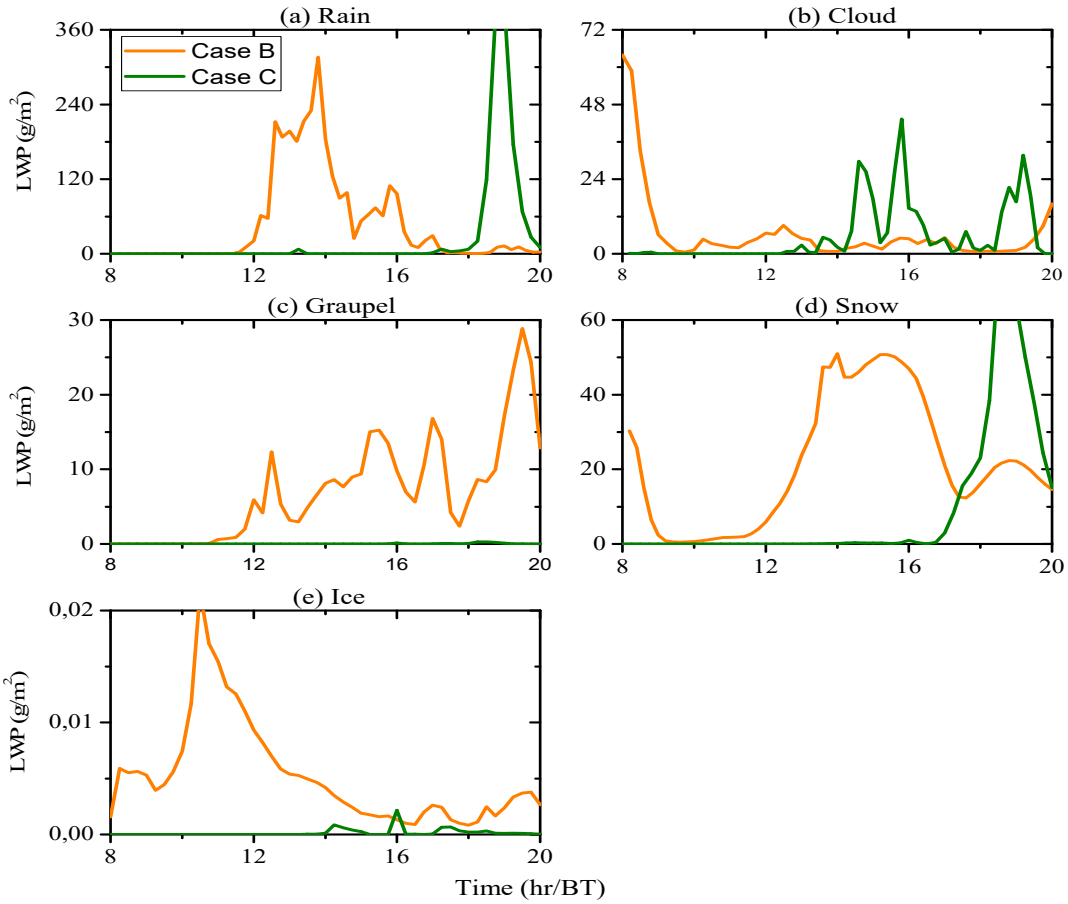

Figure 6. Time series of area-averaged hydrometeors water paths from case B and C. Case B depicted from $D0_{i=3}$ and case C from $D0_{i=5}$ represent Scenarios B and C in Table 4 from Kpaikpai et al. [54].

We observed that Scenario C did not present graupel, whereas graupel is a little abundant in Scenario B. According to Kpaikpai et al. [54], Scenarios B and C used the same microphysics scheme. The main difference in the physics setting is the planetary boundary layer scheme. Scenario B used 1D PBL parameterizations to resolve stresses and turbulent flows, assuming horizontal homogeneity. However, Scenario C ignored the latter homogeneities and included the horizontal gradients of turbulent stresses and flows, while the data from Scenario B was used to force the iteration in Scenario C. However, given the model did not produce deep cumulus clouds at the Naqu site (Scenario C), the Graupel water path cannot be included in the hydrometeors' water path statistics for Scenario C. Moreover, the ice-water path was minimal in Scenario C compared to Scenario B, while other hydrometeors' water paths seemed somewhat greater in Scenario C than in Scenario B. Therefore, more cloudy liquid water in Scenario C confirms that warm rain dominated the process. Scenario B's cloud, ice, snow, and graupel formations suggest that the mixed-phase process produced cold rain. Figures 3b and 3c have previously shown the significant heating rates resulting from mixed-phase processes in mesoscale simulations. They also show the effect on buoyancy production, which explains why cumulus clouds grow deeper. Thus, our study emphasizes the importance of mixed-phase processes, a dominant cause of uncertainty in the WRF model.

4. Summary and Conclusions

The development of a low-level baroclinic vortex in the large-scale convergence zone (33°–36°N, 84°–94°E) is critical to the dynamics of the atmospheric boundary layer (ABL) over Naqu. It has been demonstrated to disrupt the hydrological cycle across the Tibetan plateau (TP) and its surroundings. This research aims to improve our understanding of the ABL process in cumulus development over the Naqu area in TP. We conducted a thorough analysis of the interaction that occurs between the baroclinic vortex and the cumulus clouds. The study also clarified the WRF-LES model's responses to specific microphysical traits. We used data from Scenario B of Kpaikpai et al.'s [54] mesoscale study and Scenario C of their large-eddy simulation (LES). Scenario B examines the physical mechanism of vortex-cumulus interaction, whereas Scenarios B and C evaluate cloud microphysical properties. The investigation focused on Helmholtz's decomposition of the horizontal total wind vector and liquid water path to determine this interaction and its relationship to key internal forcing elements such as South Asian height (SAH) and the subtropical jet (STJ) influences.

The findings indicate that the low-level baroclinic vortex that formed in large-scale convergence zones (33°–36°N and 84°–94°E) created the necessary conditions for deep cumulus formation. However, the STJ's position at 36°N, along with the

SAH, influenced the vortex and the types of cumulus clouds that formed.

Six hours before the vortex's development, the large-scale convergence zone showed low geopotential height. This led to the formation of a low-level jet that modified the meridional circulation, transporting moisture to the convergence zone. As the vortex developed, the rotational wind exhibited counterclockwise rotation around the negative stream function within the large-scale convergence zone, indicating the presence of the vortex. The clockwise rotation of the wind's rotational component around the positive stream function at low level has revealed two subtropical highs (STHs) that developed to the southwest and southeast of the vortex, respectively. The vortex moved eastward under the effect of the STJ. However, the influence of the STH southwest of the vortex deflected the vortex southeastward of the Naqu site. The low-pressure trough between the two STHs facilitated the interaction between the meridional circulation localized southeast of Naqu and the vortex. The heating rate due to long-wave radiation revealed the cumulus congestus within the interaction zone of the vortex and eastern meridional circulation. At the upper level, the clockwise rotation of the rotational wind component around the positive stream function indicates the presence of SAH. The SAH was aligned vertically with the vortex; however, there was a little eclipse to the south due to the effect of the STJ north of it. Cumulus congestus developed just south of the SAH. During Day 3 of the model experiment, the STH, STJ, and SAH acted as sinks. The widespread subsidence across the region suggests predominantly dry weather conditions, except in the zone where cumulus congestus clouds have developed. The study emphasizes the importance of low-level baroclinity and internal forcing in determining the dynamic properties of deep cumulus clouds.

The mesoscale dynamic-microphysical interaction is one of the factors considered in this study for the numerical experiment. The difference between the two Scenarios' findings is attributed to the WRF model's spatial variability of the hydrometeors' mass concentration and planetary boundary-layer (PBL) schemes used for each Scenario. The substantial cloudy liquid water in Scenario C confirms that warm rain dominated Scenario C. Scenario B's cloud, ice, snow, and graupel formations suggest that the mixed-phase process produced cold rain. Consequently, our research highlights the significance of mixed-phase processes—a primary source of uncertainty in the WRF model—and recommends more research into the planetary boundary layer schemes currently employed in LES (Scenario C) and mesoscale simulation (Scenario B).

This model experiment demonstrated that the observation-nudging approach and one-way nesting strategies can offer accurate physical mechanisms and microphysical properties. However, the model's sensitivity to changes in horizontal and vertical resolution remains to be thoroughly documented. Indeed, from part A of this study to the current part, between Scenarios B and C, there are cases where one of the two Scenarios has prevailed over the other and shown better results. However, we recommend Scenario B to influence the results of scientific research as it provides a wider field of understanding of physical mechanisms and microphysical proprieties. Given the evolution of the WRF model from version 3.8 to version 4.5, we plan to improve horizontal and vertical resolution and use the newest planetary boundary-layer schemes to strengthen the reliability of our results. Increasing the data observed in the grey zone is also recommended to enhance the reliability of mesoscale simulation results, which must be used to improve the LES simulation's overall accuracy.

Acknowledgment:
The first author would like to thank CAS-TWAS authorities, WMO, the Togo National Meteorological Agency, and the Ministry of Higher Education of Togo for making him a meteorologist.

Funding: The Chinese Academy of Sciences (CAS) in cooperation with the World Academy of Sciences (TWAS) funded this work. This work is also highly supported by the State Program of National Natural Science of China (grant no. 41930972).

References

1. Xu X, Tang Y, Wang Y, Zhang H, Liu R, Zhou M. Triggering effects of large topography and boundary layer turbulence on convection over the Tibetan Plateau. Atmospheric Chem Phys [Internet]. 2023 Mar 15 [cited 2024 Jul 19];23(5):3299–309.
2. Chen X, Añel JA, Su Z, Torre L de la, Kelder H, Peet J van, et al. The Deep Atmospheric Boundary Layer and Its Significance to the Stratosphere and Troposphere Exchange over the Tibetan Plateau. PLOS ONE [Internet]. 2013 Feb 25 [cited 2021 May 2];8(2):e56909.
3. Fu R, Hu Y, Wright JS, Jiang JH, Dickinson RE, Chen M, et al. Short circuit of water vapor and polluted air to the global stratosphere by convective transport over the Tibetan Plateau. Proc Natl Acad Sci [Internet]. 2006 Apr 11 [cited 2021 May 2];103(15):5664–9.
4. IPCC IP on CC. Climate Change 2013 - The Physical Science Basis: Working Group I Contribution to the Fifth Assessment Report of the Intergovernmental Panel on Climate Change [Internet]. Cambridge: Cambridge University Press; 2014 [cited 2021 Apr 28].
5. Wang T, Hu C, Li N, Hou Z. Numerical analysis of ground temperature in Qinghai-Tibet Plateau. Sci China Ser E Technolgical Sci [Internet]. 2002 Aug 1 [cited 2021 Apr 29];45(4):433–43.
6. Yang K, Koike T, Fujii H, Tamura T, Xu X, Bian L, et al. The Daytime Evolution of the Atmospheric Boundary Layer and Convection over the Tibetan Plateau: Observations and Simulations. J Meteorol Soc Jpn [Internet]. 2004 [cited 2021 Mar 25];82(6):1777–92.
7. Feng X, Liu C, Fan G, Zhang J. Analysis of the structure of different Tibetan Plateau vortex types. J Meteorol Res [Internet]. 2017 Jun 1 [cited 2024 Jun 9];31(3):514–29.
8. Bracco A, Pedlosky J. Vortex Generation by Topography in Locally Unstable Baroclinic Flows. J Phys Oceanogr

[Internet]. 2003 Jan 1 [cited 2024 Jun 21];33(1):207–19.
9. Chen H, Li T, Cui J. The Reexamination of the Moisture–Vortex and Baroclinic Instabilities in the South Asian Monsoon. Atmosphere [Internet]. 2024 Feb [cited 2024 Jun 21];15(2):147.
10. Feng X, Liu C, Fan G, Liu X, Feng C. Climatology and Structures of Southwest Vortices in the NCEP Climate Forecast System Reanalysis. J Clim [Internet]. 2016 Nov 1 [cited 2021 Apr 7];29(21):7675–701.
11. Wu G, Liu Y, Zhang Q, Duan A, Wang T, Wan R, et al. The Influence of Mechanical and Thermal Forcing by the Tibetan Plateau on Asian Climate. J Hydrometeorol [Internet]. 2007 Aug 1 [cited 2021 Jul 18];8(4):770–89.
12. Duan AM, Wu GX. Role of the Tibetan Plateau thermal forcing in the summer climate patterns over subtropical Asia. Clim Dyn [Internet]. 2005 Jun 1 [cited 2021 Jun 29];24(7):793–807.
13. Li L, Yang S, Wang Z, Zhu X, Tang H. Evidence of Warming and Wetting Climate over the Qinghai-Tibet Plateau. Arct Antarct Alp Res. 2010 Nov 1;42(4):449–57.
14. Ding J, Cuo L, Zhang Y, Zhu F. Monthly and annual temperature extremes and their changes on the Tibetan Plateau and its surroundings during 1963–2015. Sci Rep. 2018 Aug 8;8(1):11860.
15. Liu X, Yin ZY, Shao X, Qin N. Temporal trends and variability of daily maximum and minimum, extreme temperature events, and growing season length over the eastern and central Tibetan Plateau during 1961–2003. J Geophys Res Atmospheres [Internet]. 2006 [cited 2021 Apr 12];111(D19).
16. Lei Y, Yao T, Yi C, Wang W, Sheng Y, Li J, et al. Glacier mass loss induced the rapid growth of Linggo Co on the central Tibetan Plateau. J Glaciol. 2012 ed;58(207):177–84.
17. Wang J, Chen X, Hu Q, Liu J. Responses of Terrestrial Water Storage to Climate Variation in the Tibetan Plateau. J Hydrol. 2020 Feb 1;584:124652.
18. Lei Y, Shi J, Xiong C, Ji D. Tracking the Atmospheric–Terrestrial Water Cycle over the Tibetan Plateau Based on ERA5 and GRACE. J Clim. 2021 Aug 1;34(15):6459–71.
19. Chen J, Wu X, Yin Y, Xiao H. Characteristics of Heat Sources and Clouds over Eastern China and the Tibetan Plateau in Boreal Summer. 2015 Sep 15 [cited 2024 Jul 19]
20. Flohn H. Contributions to a meteorology of the Tibetan highlands [Internet]. [U.S.A.]: Fort Collins, Colo. : Department of Atmospheric Science, Colorado State University, 1968.; 1968 [cited 2021 Aug 31].
21. Zhao P, Xu X, Chen F, Guo X, Zheng X, Liu L, et al. The Third Atmospheric Scientific Experiment for Understanding the Earth–Atmosphere Coupled System over the Tibetan Plateau and Its Effects. 2018 Apr 1 [cited 2024 Jul 19].
22. Charney J, Eliassen A. On the Growth of the Hurricane Depression. 1964;
23. Kuo HL. Convection in Conditionally Unstable Atmosphere. Tellus Dyn Meteorol Oceanogr [Internet]. 1961 Jan 1 [cited 2024 Jul 19];13(4):441–59.
24. Nielsen AW. Studies of CISK. Atmósfera [Internet]. 1993 [cited 2024 Jul 19];6(1).
25. Xie SP, Kubokawa A. On the Wave-CISK in the Presence of a Frictional Boundary Layer. J Meteorol Soc Jpn Ser II. 1990;68(6):651–7.
26. Lindzen RS. Wave-CISK in the Tropics. 1974 Jan 1 [cited 2024 Jul 19].
27. Liu Y, Tan ZM, Wu Z. Noninstantaneous Wave-CISK for the Interaction between Convective Heating and Low-Level Moisture Convergence in the Tropics. 2019 Jul 1 [cited 2024 Jul 19].
28. Davies HC. Phase-lagged wave-CISK. Q J R Meteorol Soc [Internet]. 1979 [cited 2024 Jul 19];105(444):325–53.
29. Li Y, An X, Fan G, Wang C, Zhao Y, Li J. Influence of Thermal Effects on Qinghai-Tibet Plateau on Air Quality in Typical Regions of China in Winter. Atmosphere [Internet]. 2020 Jan [cited 2023 Sep 30];11(1):50.
30. Tang Y, Xu G, Wan R, Wang X, Wang J, Li P. Atmospheric Thermal and Dynamic Vertical Structures of Summer Hourly Precipitation in Jiulong of the Tibetan Plateau. Atmosphere [Internet]. 2021 Apr [cited 2021 Sep 3];12(4):505.
31. Li L, Yang S, Wang Z, Zhu X, Tang H. Evidence of Warming and Wetting Climate over the Qinghai-Tibet Plateau. Arct Antarct Alp Res [Internet]. 2010 Nov 1 [cited 2021 Apr 12];42(4):449–57.
32. Tingyang D, Reiter ER. Some characteristics of cumulus convection over the Tibetan Plateau. Adv Atmospheric Sci [Internet]. 1990 Feb [cited 2021 Mar 25];7(1):87–97.
33. Sato T, Yoshikane T, Satoh M, Miura H, Fujinami H. Resolution Dependency of the Diurnal Cycle of Convective Clouds over the Tibetan Plateau in a Mesoscale Model. J Meteorol Soc Jpn Ser II. 2008;86A:17–31.
34. Luo Y, Zhang R, Qian W, Luo Z, Hu X. Intercomparison of Deep Convection over the Tibetan Plateau–Asian Monsoon Region and Subtropical North America in Boreal Summer Using CloudSat/CALIPSO Data. J Clim [Internet]. 2011 Apr 15 [cited 2021 Mar 25];24(8):2164–77.
35. Lu C, Liu Y, Zhang G, wu X, Endo S, Cao L, et al. Improving Parameterization of Entrainment Rate for Shallow Convection with Aircraft Measurements and Large Eddy Simulation. J Atmospheric Sci. 2015 Nov 11;73:151111130909008.
36. Dong W, Lin Y, Wright JS, Ming Y, Xie Y, Wang B, et al. Summer rainfall over the southwestern Tibetan Plateau controlled by deep convection over the Indian subcontinent. Nat Commun [Internet]. 2016 Mar 7 [cited 2021 Apr 16];7(1):10925.
37. Zhao Y, Wang M, Huang A, Li H, Huo W, Yang Q. Relationships between the West Asian subtropical westerly jet and summer precipitation in northern Xinjiang. Theor Appl Climatol [Internet]. 2014 May 1 [cited 2022 Jun 12];116(3):403–11.
38. Wei W, Zhang R, Wen M, Yang S. Relationship between the Asian Westerly Jet Stream and Summer Rainfall over Central Asia and North China: Roles of the Indian Monsoon and the South Asian High. J Clim [Internet]. 2017 Jan 15 [cited 2022 Jun 11];30(2):537–52.
39. Zhao P, Li Y, Guo X, Xu X, Liu Y, Tang S, et al. The Tibetan Plateau Surface-Atmosphere Coupling System and Its Weather and Climate Effects: The Third Tibetan Plateau Atmospheric Science Experiment. J Meteorol Res

[Internet]. 2019 Jun 1 [cited 2024 May 10];33(3):375–99.
40. Li P, Furtado K, Zhou T, Chen H, Li J. Convection-permitting modelling improves simulated precipitation over the central and eastern Tibetan Plateau. Q J R Meteorol Soc [Internet]. 2021 [cited 2021 Jun 27];147(734):341–62.
41. Ren R, Zhu C, Cai M. Linking quasi-biweekly variability of the South Asian high to atmospheric heating over Tibetan Plateau in summer. Clim Dyn [Internet]. 2019 Sep 1 [cited 2021 Aug 22];53(5):3419–29.
42. Shang W, Ren X, Huang B, Cubasch U, Yang XQ. Subseasonal intensity variation of the South Asian high in relationship to diabatic heating: observation and CMIP5 models. Clim Dyn [Internet]. 2019 Feb 1 [cited 2021 May 5];52(3):2413–30.
43. Sato T. Influences of subtropical jet and Tibetan Plateau on precipitation pattern in Asia: Insights from regional climate modeling. Quat Int [Internet]. 2009 Feb 1 [cited 2022 Jun 10];194(1):148–58.
44. Chen X, Škerlak B, Rotach MW, Añel JA, Su Z, Ma Y, et al. Reasons for the Extremely High-Ranging Planetary Boundary Layer over the Western Tibetan Plateau in Winter. J Atmospheric Sci [Internet]. 2016 May 1 [cited 2021 Mar 25];73(5):2021–38.
45. Li Y, Zhang M. Cumulus over the Tibetan Plateau in the Summer Based on CloudSat–CALIPSO Data. J Clim [Internet]. 2016 Feb 1 [cited 2022 May 10];29(3):1219–30.
46. Hunt KMR, Curio J, Turner AG, Schiemann R. Subtropical Westerly Jet Influence on Occurrence of Western Disturbances and Tibetan Plateau Vortices. Geophys Res Lett [Internet]. 2018 [cited 2021 May 4];45(16):8629–36.
47. Wu L, Feng X, Liang M. Insensitivity of the Summer South Asian High Intensity to a Warming Tibetan Plateau in Modern Reanalysis Datasets. J Clim [Internet]. 2017 Apr 15 [cited 2021 May 5];30(8):3009–24.
48. Wei HH, Bordoni S. On the Role of the African Topography in the South Asian Monsoon. J Atmospheric Sci [Internet]. 2016 Aug 1 [cited 2023 Jul 31];73(8):3197–212.
49. Fu Y, Ma Y, Zhong L, Yang Y, Guo X, Wang C, et al. Land-surface processes and summer-cloud-precipitation characteristics in the Tibetan Plateau and their effects on downstream weather: a review and perspective. Natl Sci Rev [Internet]. 2020 Mar 1 [cited 2021 Apr 11];7(3):500–15.
50. Zhou Y, Li D, Liu H, Li X. Diurnal Variations of the Flux Imbalance Over Homogeneous and Heterogeneous Landscapes. Bound-Layer Meteorol [Internet]. 2018 Sep [cited 2021 Jun 27];168(3):417–42.
51. Wang X, Pang G, Yang M. Precipitation over the Tibetan Plateau during recent decades: a review based on observations and simulations. Int J Climatol [Internet]. 2018 [cited 2021 Sep 1];38(3):1116–31.
52. Ma Y, Wang B, Chen X, Zhong L, Hu Z, Ma W, et al. Strengthening the three-dimensional comprehensive observation system of multi-layer interaction on the Tibetan Plateau to cope with the warming and wetting trend. Atmospheric Ocean Sci Lett [Internet]. 2022 Jul 1 [cited 2022 Jun 18];15(4):100224.
53. Son JH, Seo KH, Wang B. How Does the Tibetan Plateau Dynamically Affect Downstream Monsoon Precipitation? Geophys Res Lett [Internet]. 2020 [cited 2021 Apr 12];47(23):e2020GL090543.
54. Kpaikpai B, Sun J, Zhu J, Banna M, Ogou FK, Vuguziga F, et al. Mesoscale and Large-Eddy Simulation of the Boundary Layer Process of Cumulus Development over Naqu, Tibetan Plateau Part A: Comparison Between Simulation and Observation. Space Sci J [Internet]. 2024 May 31 [cited 2024 Jun 2];1(2):1–18.
55. Skamarock WC, Klemp JB, Dudhia J, Gill DO, Barker DM, Duda MG, et al. A Description of the Advanced Research WRF Version 4. 2019 Jan 9 [cited 2023 Aug 2].
56. Qian X, Yao Y, Wang H, Zou L, Li Y, Yin J. Validation of the WRF Model for Estimating Precipitable Water Vapor at the Ali Observatory on the Tibetan Plateau. Publ Astron Soc Pac [Internet]. 2020 Nov [cited 2021 Jun 27];132(1018):125003.
57. Qian X, Yao Y, Zou L, Wang H, Yin J, Li Y. Modelling of atmospheric optical turbulence with the Weather Research and Forecasting model at the Ali observatory, Tibet. Mon Not R Astron Soc [Internet]. 2021 Jul 21 [cited 2021 Jun 27];505(1):582–92.
58. Bladel JV. A Discussion of Helmholtz' Theorem. Electromagnetics [Internet]. 1993 Jan 1 [cited 2021 Jul 18];13(1):95–110.
59. Campisi M. On the mechanical foundations of thermodynamics: The generalized Helmholtz theorem. Stud Hist Philos Sci Part B Stud Hist Philos Mod Phys [Internet]. 2005 Jun 1 [cited 2021 Jul 18];36(2):275–90.
60. Fuelberg HE, Browning PA. Roles of Divergent and Rotational Winds in the Kinetic Energy Balance Intense Convective Activity. Mon Weather Rev [Internet]. 1983 Nov 1 [cited 2021 Jul 18];111(11):2176–93.
61. Glötzl E, Richters O. Helmholtz Decomposition and Rotation Potentials in n-dimensional Cartesian Coordinates. ArXiv201213157 Math-Ph [Internet]. 2021 Feb 19 [cited 2021 Jul 18].
62. Browning KA. Cloud dynamics. By Robert A. Houze, Jr. Academic Press 1993. Pp. 573. Hardback $149.00. Paperback $54.95. ISBN 0-12-356880-3. Q J R Meteorol Soc [Internet]. 1994 [cited 2021 Aug 7];120(519):1427–8.
63. Groemer H. Geometric Applications of Fourier Series and Spherical Harmonics. 1st ed. Cambridge ; New York: Cambridge University Press; 1996. 344 p.
64. Hammond M, Lewis NT. The rotational and divergent components of atmospheric circulation on tidally locked planets. Proc Natl Acad Sci [Internet]. 2021 Mar 30 [cited 2021 Jul 21];118(13).
65. Higuchi A. Symmetric tensor spherical harmonics on the N-sphere and their application to the de Sitter group SO(N,1). J Math Phys [Internet]. 1998 Jun 4 [cited 2021 Jul 20];28(7):1553.
66. Tribbey W. Numerical Recipes: The Art of Scientific Computing (3rd Edition) is written by William H. Press, Saul A. Teukolsky, William T. Vetterling, and Brian P. Flannery, and published by Cambridge University Press, © 2007, hardback, ISBN 978-0-521-88068-8, 1235 pp. ACM SIGSOFT Softw Eng Notes [Internet]. 2010 Nov 27 [cited 2021 Jul 20];35(6):30–1.

67. Bierdel LB. On the relevance of rotational and divergent modes of motion to mesoscale dynamics and upscale error growth [Internet] [Text.PhDThesis]. Ludwig-Maximilians-Universität München; 2017 [cited 2021 Jul 19].
68. Emanuel KA. Overview of Atmospheric Convection. In: Smith RK, editor. The Physics and Parameterization of Moist Atmospheric Convection [Internet]. Dordrecht: Springer Netherlands; 1997 [cited 2021 May 31]. p. 1–28. (NATO ASI Series).
69. Houze AR. Cloud Dynamics [Internet]. 1rst ed. Dmowska R, editor. Elsevier, Academic Press; 1993. 573 p. (International Geophysics; vol. 53).
70. Smith RK, editor. The Physics and Parameterization of Moist Atmospheric Convection [Internet]. Springer Netherlands; 1997 [cited 2021 Jul 10]. (Nato Science Series C:).
71. Wallace JM, Hobbs PV. Atmospheric Science: An Introductory Survey. Elsevier; 2006. 505 p.
72. Adams-Selin RD, Heever SC van den, Johnson RH. Impact of Graupel Parameterization Schemes on Idealized Bow Echo Simulations. Mon Weather Rev [Internet]. 2013 Apr 1 [cited 2022 Jun 23];141(4):1241–62.
73. Tsonis A. An Introduction to Atmospheric Thermodynamics [Internet]. 2nd ed. Cambridge: Cambridge University Press; 2007 [cited 2021 Jul 7].
74. Yano JI, Ambaum MHP. Moist static energy: definition, reference constants, a conservation law and effects on buoyancy: Moist Static Energy. Q J R Meteorol Soc [Internet]. 2017 Oct [cited 2021 Jul 12];143(708):2727–34.
75. Xiang J, Zhou J, Huang S. The boundary layer height obtained by the spline numerical differentiation method using COSMIC GPS radio occultation data: A case study of the Qinghai-Tibet Plateau. J Atmospheric Sol-Terr Phys [Internet]. 2021 Apr 1 [cited 2021 Apr 18];215:105535.
76. Kotthaus S, Grimmond CSB. Atmospheric boundary-layer characteristics from ceilometer measurements. Part 1: A new method to track mixed layer height and classify clouds. Q J R Meteorol Soc [Internet]. 2018 [cited 2021 Mar 25];144(714):1525–38.
77. Seethala C, Horváth Á. Global assessment of AMSR-E and MODIS cloud liquid water path retrievals in warm oceanic clouds. J Geophys Res Atmospheres [Internet]. 2010 [cited 2022 Jun 23];115(D13).
78. Stull RB. An Introduction to Boundary Layer Meteorology [Internet]. Springer Netherlands; 1988 [cited 2021 May 10]. (Atmospheric and Oceanographic Sciences Library).
79. Proctor FH. The Terminal Area Simulation System. Volume 1: Theoretical Formulation. Langley Research Center; 1987. 180 p.
80. Straka JM. Cloud and Precipitation Microphysics: Principles and Parameterizations [Internet]. Cambridge: Cambridge University Press; 2009 [cited 2021 Jul 7].
81. Pruppacher HR, Klett JD. Microphysics of Clouds and Precipitation [Internet]. 2nd ed. Springer Netherlands; 2010 [cited 2021 Jul 7]. (Atmospheric and Oceanographic Sciences Library).
82. Yan Y, Liu Y, Lu J. Cloud vertical structure, precipitation, and cloud radiative effects over Tibetan Plateau and its neighboring regions. J Geophys Res Atmospheres [Internet]. 2016 [cited 2021 Apr 19];121(10):5864–77.
83. Emanuel KA. Overview of Atmospheric Convection. In: Smith RK, editor. The Physics and Parameterization of Moist Atmospheric Convection [Internet]. Dordrecht: Springer Netherlands; 1997 [cited 2021 May 31]. p. 1–28. (NATO ASI Series).
84. Smith RK, editor. The Physics and Parameterization of Moist Atmospheric Convection [Internet]. Springer Netherlands; 1997 [cited 2021 Jul 10]. (Nato Science Series C:).
85. Lu C, Liu Y, Zhang GJ, Wu X, Endo S, Cao L, et al. Improving Parameterization of Entrainment Rate for Shallow Convection with Aircraft Measurements and Large-Eddy Simulation. J Atmospheric Sci [Internet]. 2016 Feb 1 [cited 2024 Jun 9];73(2):761–73.